UNIVERSITY
OF TRENTO

DIPARTIMENTO DI INGEGNERIA E SCIENZA DELL'INFORMAZIONE

38123 Povo – Trento (Italy), Via Sommarive 14
http://www.disi.unitn.it

BROADBAND HIGH DIRECTIVITY MULTI-BEAM EMISSION THROUGH TRANSFORMATION OPTICS ENABLED METAMATERIAL LENSES

Zhi Hao Jiang, Micah D. Gregory, and Douglas H. Werner

August 2012

Technical Report # DISI-12-030

***Abstract*—A new broadband two- and three-dimensional, polarization independent embedded coordinate transformation is introduced that is capable of mapping the radiation from an embedded omnidirectional source into any desired number of highly directive beams pointed in arbitrary directions. This transformation requires anisotropic materials, yet is spatially invariant and thereby can be readily implemented by currently existing metamaterial technologies. Moreover, the performance of the transformation is not sensitive to small material parameter variations, thus enabling a broad operational bandwidth. To validate the concept, a broadband 3D coordinate transformation metamaterial lens fed by a simple monopole antenna was designed, fabricated and characterized, achieving a quad-beam radiation pattern over a 1.26:1 bandwidth with approximately 6 dB realized gain improvement in the *H*-plane. In addition, the near-field coupling between the monopole and the lens was carefully tuned to accomplish a remarkable 70% broadening of the impedance bandwidth compared to the monopole antenna operating alone. It is also shown from the field simulations that the realized metamaterial lens provides both near-field and far-field 3D collimating effects.**

***Index Terms*—Antennas, broadband, capacitively-loaded ring resonator, highly directive, metamaterials, monopole, multiple beam, transformation optics**

I. Introduction

The field of transformation optics [1], [2], sometimes referred to as transformation electromagnetics [3], has witnessed dramatic development ever since it was proposed by Pendry *et al.* and Leonhardt in 2006. This technique provides engineers and scientists with unprecedented ability to manipulate the propagation and radiation of electromagnetic waves. The design approach was made possible by the fact that Maxwell's equations can be written in a form-invariant manner under coordinate transformations, where only the permittivity and permeability tensors are changed [4], [5]. In this way, the electromagnetic waves in one coordinate system (*x*, *y*, *z*) can be described as if propagating in another different coordinate system (*x′*, *y′*, *z′*) with the coordinate transformation function *x′=x′(x*, *y*, *z*)*, y′=y′(x*, *y*, *z*)*, z′=z′(x*, *y*, *z*) applied to the permittivity and permeability tensors. To design an electromagnetic transformation, one first defines the desired wave propagation characteristics in a virtual space (x, y, z) with the constitutive parameter tensors denoted as $\bar{\bar{\varepsilon}}(x, y, z)$ and $\bar{\bar{\mu}}(x, y, z)$. Next, the designer finds a physical space (x', y', z') with the constitutive parameter tensors denoted as $\bar{\bar{\varepsilon}}'(x', y', z')$ and $\bar{\bar{\mu}}'(x', y', z')$ which are unknown. In order to keep the same wave propagation characteristics with that of the virtual space, the material parameter tensors of the physical space can be calculated in the last step by

$$\bar{\bar{\varepsilon}}' = \frac{A\bar{\bar{\varepsilon}}A^{\mathrm{T}}}{\det(A)} \text{ and } \bar{\bar{\mu}}' = \frac{A\bar{\bar{\mu}}A^{\mathrm{T}}}{\det(A)}, \qquad (1)$$

where A is the Jacobian transformation matrix between the virtual space and the physical space.

Over the past five years, the transformation optics approach has been extensively exploited to create a wide variety of novel, and otherwise unattainable, electromagnetic devices. The most well-known one of these is the electromagnetic invisibility cloak [1], [6], [7], which is designed to bend the waves around a region of space so that the object hidden inside the region is exempt from being detected by the scattered fields. Other intriguing transformation optics examples have also been theoretically proposed and numerically examined including field rotators [8], [9], polarization splitters [9], [10], electromagnetic concentrators [11], [12], wave collimators [13]-[17], beam benders [15], [18], illusion devices [19], [20], flat-reflectors [21], and many others. Moreover, the rapid progress of metamaterial technology provides various sub-wavelength resonating/non-resonating metamaterial unit cells with exotic anisotropic/isotropic effective material parameters [22], [23] required by most of these transformation optics designs. As a result, a few of these transformation optics devices have been implemented and experimentally demonstrated [6], [8], [20]. However, the majority of these designs are still constrained to the realm of purely mathematical constructions with associated numerical verifications, and for most experimentally demonstrated examples, are limited to operate within a fairly narrow frequency range. This is primarily due to two limitations, the first of which is inhomogeneous material parameters with a high degree of sensitivity to the spatially dependent permittivity and permeability tensors on a sub-wavelength scale. The second is strong anisotropy of the material parameters which sometimes requires permittivity and permeability tensors with extreme values.

Several efforts have been carried out in recent years that attempt to circumvent these shortcomings by sacrificing certain types of functionality. One major achievement was the employment of quasi-conformal mappings, eliminating the material anisotropy and allowing implementation using purely isotropic dielectrics [24]. Although this has the disadvantage of inhomogeneous material parameters and a degraded impedance match at the interface between free space and the transformed medium, this approach enables devices with broader bandwidth and low losses, such as the carpet cloaks [25],

[26], Luneburg lenses [27], [28], as well as beam benders [29]. More recently, two works on macroscopic cloaks have suggested alternative methods for design simplification, which involve the use of coordinate transformations that require anisotropic yet spatially invariant material parameters [30], [31]. Although these cloaks operate over a limited range of incident azimuthal angles, they demonstrate the potential for using simple embedded coordinate transformations to design devices that have straightforward implementation.

With the vital growth of wireless networks and the increasing complexity of their environments, highly directive antennas with multiple main beams and a single feed are found to be useful for various wireless communication systems such as base station antennas, multiple-input multiple-output (MIMO) systems, automotive radar systems, point/multipoint-to-point radios, and so on [32]-[34]. Instead of omnidirectional or unidirectional radiation patterns, customized multiple main beams can provide more flexibility in avoiding obstacles in urban areas while providing stronger signal intensity in directions where receiver clusters are located. Having the ability to produce multiple highly collimated beams with a single feed antenna is also desirable for maintaining ease of implementation. Thus far, several different techniques have been reported for improving the directivity and/or increasing the number of beams radiated by an antenna. Several two dimensional coordinate mappings based on the transformation optics approach were investigated that are capable of effectively converting a cylindrical wave into a collimated plane wave [13]-[17]. However, these designs all require inhomogeneous anisotropic material parameters with extreme values, thus not leading themselves to practical realization or broadband applications. Other methodologies such as the Fabry-Perot (FP) cavities [35], [36] and artificial magnetic conducting (AMC) substrates [37] have also been used to increase the directivity of an embedded source. The operation of the FP cavities is based on the constructive phase addition of the transmitted and reflected waves from the multilayer structures, whereas the advantage of the AMC substrates is their unique near-zero reflection phase. These AMC substrates can also be used to replace the ground plane in a FP cavity for miniaturization purposes [38]. Alternatively, electromagnetic band gap (EBG) structures can be applied to increase the directivity of low profile patch and wire antennas as a result of the suppressed surface waves propagating on these EBG structures [39], [40]. Recently, it has been proposed to use bulk zero-index metamaterials [41], [42] and anisotropic low-index metamaterials [43]-[46] to achieve directive emission from an embedded antenna. Nevertheless, most of these approaches, when applied to an actual antenna, either have only a narrow bandwidth with improved directivity or suffer from a high return loss which deteriorates the realized gain. At the same time, a majority of these approaches are also limited to providing only one or two radiated beams and thus are not suitable for multi-beam radiation.

In this paper, we extend the idea of a simple embedded coordinate transformation which requires only anisotropic homogeneous material parameters for the design of highly directive multi-beam antenna lenses. Notably, the technique proposed here is capable of converting the radiation from an embedded omnidirectional source into any number of highly directive beams, each radiating in an arbitrary direction within a broad bandwidth. We first describe the polarization independent two- and three-dimensional embedded coordinate transformations that require only simple material parameters for directive emission, along with several numerical examples. The wave propagation properties inside the transformed medium are also studied by examining the equations that govern the dispersion relation. In Section III, a broadband transformation optics metamaterial lens is designed to generate a quad-beam radiation pattern from a simple embedded monopole with efficient operation over a broad bandwidth. The experimental measurements of the monopole with and without the lens will be presented therein. The effects of changing the lens dimensions are discussed in Section IV. Conclusions and future efforts will be provided in Section V.

II. Two/Three-Dimensional Coordinate Transformation for Highly Directive Emission

In this section, we present the analytical expressions of the proposed embedded coordinate transformations for directive emission in both two and three dimensions. Corresponding full-wave simulations using homogeneous lenses will also be provided as numerical validations.

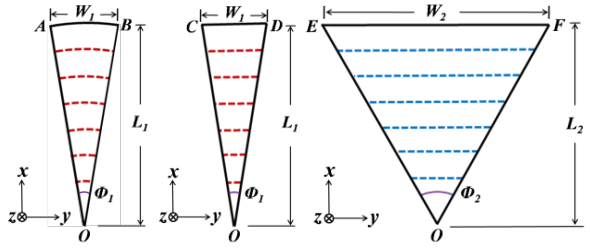

Fig. 1. Two dimensional directive emission coordinate transformation. (a) Geometry of the fan-shaped virtual space. (b) Geometry of the simplified triangular virtual space. (c) Geometry of the triangular physical space.

A. Two Dimensional Case

We first consider a two-dimensional directive emission transformation, where the fields are restricted to be invariant along the *z*-direction [47]. The schematic of the embedded coordinate transformation is shown in Fig.1 where an air-filled, fan-shaped virtual space with a central angle of Φ_1 (see Fig. 1(a)) is mapped to an isosceles triangle with a vertex angle of Φ_2 in the physical space (see Fig. 1(c)) which has material parameters denoted by $\bar{\bar{\varepsilon}}_r'(x', y')$ and $\bar{\bar{\mu}}_r'(x', y')$. An isotropic line source is located at the center (point *O*), with either the electric field or magnetic field along the *z*-direction, representing the transverse electric (*TE*) or transverse magnetic (*TM*) polarization, respectively. Note that the value of Φ_1 should be much smaller than the value of Φ_2 to correspond to high directivity in the virtual space. Since the equi-amplitude, equi-phase lines of the virtual space are a set of parallel arcs while those of the physical space are a set of parallel straight lines, a direct mapping from the fan region to the triangular region will inevitably result in spatial dependent anisotropic transformed material parameters. This is caused by the nonlinearity of the point-to-point mapping relation between the virtual and physical spaces as shown in several previously reported cylindrical-to-plane wave source transformation designs [13]-[15].

To reduce the unwanted spatial dependency of the transformed material parameters in the physical space, a geometrical simplification can be applied to the virtual space geometry. Since the value of Φ_1 is small, the fan region can be approximated by an isosceles triangle with the same central angle as shown in Fig. 1(b). Thus, an intermediate space which possesses a linear geometrical similarity with the physical space can be inserted into the transformation process to simplify the transformed material parameters. Now, the transformation can be written as

$$\begin{cases} x' = L_2 x / L_1 \\ y' = W_2 y / W_1 \\ z' = z \end{cases} \tag{2}$$

where (x, y, z) and (x', y', z') denote the coordinates of the virtual and physical space, respectively. By virtue of the metric invariance of Maxwell's equations, the relative permittivity and permeability tensors of the transformed medium in the physical space can be expressed as

$$\bar{\bar{\varepsilon}}_r' = \bar{\bar{\mu}}_r' = \begin{bmatrix} L_2 W_1 / L_1 W_2 & 0 & 0 \\ 0 & L_1 W_2 / L_2 W_1 & 0 \\ 0 & 0 & L_1 W_1 / L_2 W_2 \end{bmatrix}. \tag{3}$$

These tensor parameters can be divided into two groups (μ_{rx}', μ_{ry}', ε_{rz}' and ε_{rx}', ε_{ry}', μ_{rz}') which are active under the *TE* and *TM* polarization, respectively. As Maxwell's equations show, the dispersion relations and the wave trajectory in the physical space remain the same provided that $\mu_{rx}'\varepsilon_{rz}'$, $\mu_{ry}'\varepsilon_{rz}'$, $\mu_{rz}'\varepsilon_{rx}'$, and $\mu_{rz}'\varepsilon_{ry}'$ are held constant [48]. Thus, the material tensor expressions can be scaled to

$$\bar{\bar{\varepsilon}}_r' = \bar{\bar{\mu}}_r' = \mathrm{diag}[(W_1/W_2)^2, (L_1/L_2)^2, 1]. \tag{4}$$

Since the radiated beam is highly directive in the *x*-direction which is perpendicular to the interface between the transformed medium and free space, we further let $L_1 = L_2$ so that the impedance is matched on the interface. The relative permittivity and permeability tensors can then be written as

$$\bar{\bar{\varepsilon}}_r' = \bar{\bar{\mu}}_r' = \mathrm{diag}[(W_1/W_2)^2, 1, 1] \tag{5}$$

where each requires only one parameter possessing a low value.

It should be noted that a previously reported conformal mapping enabled collimating lens [45] is actually a special case of the coordinate transformation proposed here when we set $L_1 W_1 = L_2 W_2$ in (3). In this sense, (3) is a general expression for achieving directive emission with homogenous anisotropic medium and can be simplified to transformed media with different anisotropy.

In addition, by applying the coordinate rotation transformation [49] to the above directive emission transformation, more advanced highly directive multi-beam lenses can be synthesized by surrounding the embedded isotropic source with several triangular segments. Importantly, this type of lens can provide an arbitrary number of collimated beams, each radiating in a prescribed direction. As shown in Fig. 2(a), the material tensors of each lens segment can be expressed as

$$\bar{\bar{\varepsilon}}_r{}' = \bar{\bar{\mu}}_r{}' = \begin{bmatrix} \frac{W_1^2}{W_2^2}cos^2\phi_n + sin^2\phi_n & (\frac{W_1^2}{W_2^2} - 1)cos\phi_n sin\phi_n & 0 \\ (\frac{W_1^2}{W_2^2} - 1)cos\phi_n sin\phi_n & \frac{W_1^2}{W_2^2}sin^2\phi_n + cos^2\phi_n & 0 \\ 0 & 0 & 1 \end{bmatrix} \quad (6)$$

Even though the mathematical expression contains non-zero off-diagonal tensor parameters, the medium can be implemented by rotating the directions of the subwavelength metamaterial building block resonators.

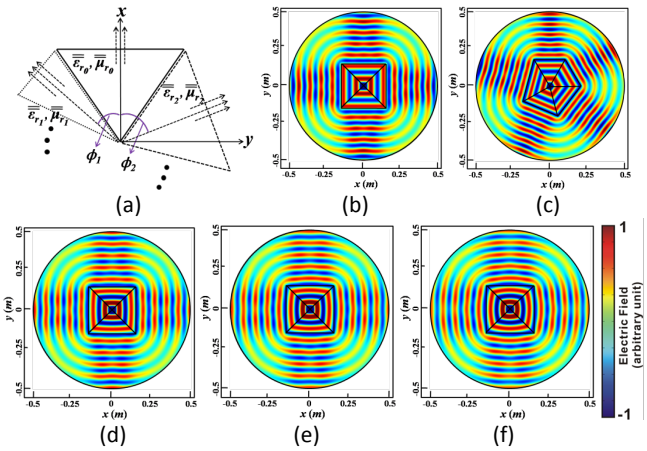

Fig. 2. (a) Configuration of multiple rotated lens segments to produce multi-beam radiation. Snapshots of the *z*-directed near- and far-zone electric field determined via a 2D COMSOL simulation of the transformation optics lens at 3 GHz (b) with four radiated beams uniformly distributed and (c) five radiated beams non-uniformly distributed in the *x*-*y* plane. Note that in both cases the corresponding $\bar{\bar{\mu}}_r{}'$ parameter in the direction of the radiated beam has a magnitude of 0.01 for each segment of the lens. 2D COMSOL simulations of a similar lens to (b) but when the corresponding $\bar{\bar{\mu}}_r{}'$ parameter in the direction of the radiated beam has a magnitude of (d) 0.1, (e) 0.2 and (f) 0.3 for each segment of the lens.

To validate the concept, two-dimensional full-wave simulations were carried out using COMSOL finite element solver [50]. For simplicity, only *TE* polarization with a *z*-directed *E*-field was used in the simulations. Considering the outer radiation boundary is 5λ away from the source, these simulations exhibit both the near- and far-field behaviors of the lenses. The first lens has four collimated beams uniformly distributed in the *x*-*y* plane pointing at ϕ = {0°, 90°, 180°, 270°} as shown in Fig. 2(b). To demonstrate the flexibility of controlling the radiated beams, a second lens is displayed in Fig. 2(c) having five customized collimated beams, each radiating at the desired angles of ϕ = {30°, 90°, 165°, 247.5°, 322.5°}. Both lenses have a low-value $\bar{\bar{\mu}}_r{}'$ parameter with a magnitude of 0.01 for each of the segments. From the electric field distribution, it is observed that the waves radiated from the central isotropic source are well-collimated, even in close proximity to the source. To study the impact of the variations in the material parameter values on the lens performance, three additional quad-beam lenses similar to the one shown in Fig. 2(b) were simulated with the magnitude of the $\bar{\bar{\mu}}_r{}'$ parameter in the direction of the radiated beams set to be 0.1, 0.2, and 0.3 for each lens segment. As presented in Fig. 2(d)-2(f), the beam width of the lenses broadens as the magnitude of the corresponding $\bar{\bar{\mu}}_r{}'$ parameter increases, however, the lenses are still able to maintain highly directive beams in the four desired directions. Since most metamaterial realizations of effective media are less dispersive in the low index band which is on the resonance tail [51], the insensitivity of material parameters makes this type of transformation optics lens suitable for broadband applications.

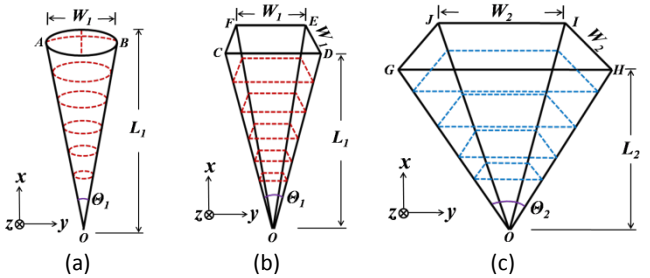

Fig. 3. Three-dimensional directive emission coordinate transformation. (a) Geometry of the spherical cone shaped virtual space. (b) Geometry of the simplified square pyramid shaped virtual space. (c) Geometry of the square pyramid shaped physical space.

B. Three Dimensional Case

The transformations introduced in the previous sub-section provide us the freedom to manipulate both the number and the directions of highly directive radiated beams in two-dimensions. In certain applications, however, multi-beam radiation is desired with beams pointing at specific directions in three dimensions. To fulfill this potential design requirement, the three-dimensional coordinate transformation and associated numerical validations are also provided. As shown in Fig. 3(a), the virtual space is an air-filled, spherical cone with a cone angle of Θ_1. It is mapped to a square pyramid with an apex angle of Θ_2 in the physical space (see Fig. 3(c)) which has material parameters denoted by $\bar{\bar{\varepsilon}}_r'(x', y', z')$ and $\bar{\bar{\mu}}_r'(x', y', z')$. Similar to the two-dimensional case, the direct mapping between the virtual and physical spaces is not a linear transformation, thus leading to inhomogeneous anisotropic material parameters with extreme values. Here, we can also make a geometrical approximation by using a square pyramid with an apex angle Θ_1 the same as the virtual space (see Fig. 3(b)). The coordinate transformation can thus be expressed as

$$\begin{cases} x' = L_2 x / L_1 \\ y' = W_2 y / W_1 \\ z' = W_2 z / W_1 \end{cases} \tag{7}$$

where (x, y, z) and (x', y', z') are the coordinates of the virtual and physical space, respectively. Like the two-dimensional case, simplification can also be made to match the impedance of the transformed medium to free space for the directive radiating beam. The resulting relative permittivity and permeability tensors of the transformed medium are again

$$\bar{\bar{\varepsilon}}_r' = \bar{\bar{\mu}}_r' = \mathrm{diag}[(W_1/W_2)^2, 1, 1]. \tag{8}$$

Similarly, a highly directive multi-beam transformation optics lens can be formed by applying the 3-D coordinate rotation mapping [49] to the material tensors of each lens segment. This type of lens can convert the radiation from an embedded isotropic source to a customized radiation pattern in three dimensions. As an example, we surrounded a previously reported quasi-isotropic radiator [52] shown in Fig. 4(a) with six lens segments, each having low-value $\bar{\bar{\varepsilon}}_r$ and $\bar{\bar{\mu}}_r$ parameters with a magnitude of 0.01 in the direction of the radiated beam. Fig. 4(b) shows the 3D radiation patterns with and without the presence of the transformation optics lens simulated by Ansoft HFSS™ finite element solver [53]. We can observe that the antenna alone has a near-isotropic radiation pattern, whereas with the lens present, the radiation pattern exhibits six highly directive beams. It should be noted that not all of the six directive beams have the same linear polarization, which is due to the quasi-isotropic source antenna employed here and not the transformation optics lens since its response is polarization independent.

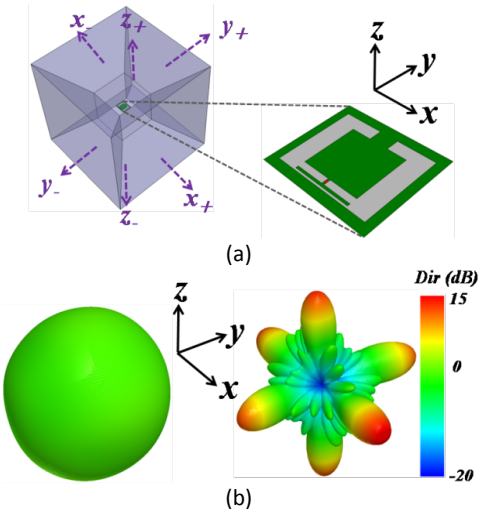

Fig. 4. Three dimensional coordinate transformation lens applied to a quasi-isotropic antenna proposed in [52]. (a) The three dimensional directive emission lens and the embedded quasi-isotropic antenna. The lens is designed to produce six highly directive beams; one normal to each face of the lens as indicated by the labels. (b) The HFSS simulated radiation pattern of the quasi-isotropic antenna without (left) and with (right) the lens.

C. *Wave Propagation in the Transformed Medium*

To obtain a better understanding of the characteristics of wave propagation inside the transformed medium and why a medium with one low-value permittivity and permeability tensor parameter would lead to directive emission, it is helpful to consider the dispersion relationship in the medium. Suppose we assume the transformed anisotropic medium has diagonal-only constitutive permittivity and permeability tensors given by

$$\overline{\overline{\varepsilon_{tr}}} = \varepsilon_0 \mathrm{diag}[\varepsilon_{trx}, \varepsilon_{try}, \varepsilon_{trz}] \qquad (9a)$$

and

$$\overline{\overline{\mu_{tr}}} = \mu_0 \mathrm{diag}[\mu_{trx}, \mu_{try}, \mu_{trz}], \qquad (9b)$$

where ε_0 and μ_0 are the permittivity and permeability of free space, respectively. A two-dimensional problem can be decomposed into *TE* polarization with electric field along the *z*-direction and *TM* polarization with magnetic field along the *z*-direction. Under these conditions the dispersion relations can be separated for each polarization and written as

$$\beta_{TEy}^2/\mu_{trx} + \beta_{TEx}^2/\mu_{try} = k_0^2 \varepsilon_{trz} \qquad (10a)$$

and

$$\beta_{TMy}^2/\varepsilon_{trx} + \beta_{TMx}^2/\varepsilon_{try} = k_0^2 \mu_{trz}, \qquad (10b)$$

where k_0 is the free space wave number and $\beta_{TE(TM)x}$ and $\beta_{TE(TM)y}$ are the *x*- and *y*-components of the wave number in the material for *TE* and *TM* polarizations, respectively. When ε_{trx} and μ_{trx} have small near-zero magnitudes while other tensor parameters possess positive values equal to or larger than unity (as dictated by the coordinate transformations), β_{TEy} and β_{TMy} are limited to be small in order to satisfy the two dispersion relations given in (10). This indicates that inside the transformed medium, the waves are forced to propagate close to the *x*-direction with a very small *y*-component in the wave vector. The behavior is confirmed in Fig. 2(b)-(f), where the waves are collimated not only in the far-field, but also in the near-field region inside each lens segment, even in close proximity to the source.

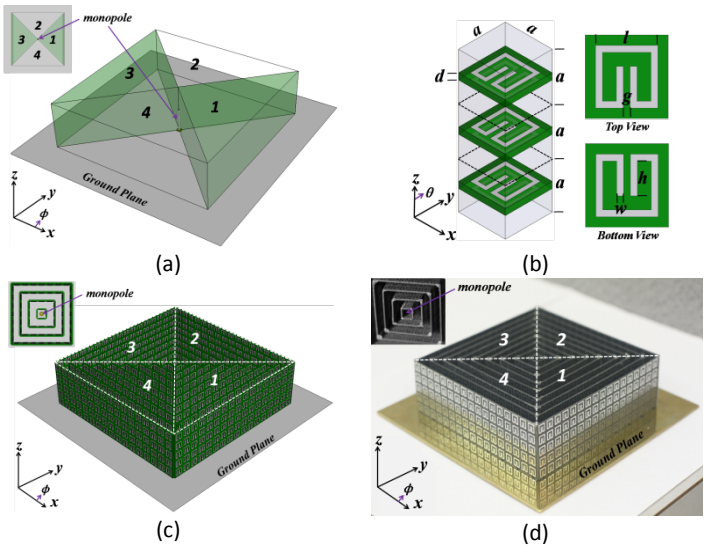

Fig. 5. (a) Conceptual configuration of the lens surrounding a monopole antenna. (b) Unit cell geometry. The dimensions are *a=6mm*, *d=0.76mm*, *l=4.5mm*, *g=0.5mm*, *w=0.5mm* and *h=2.5mm*. Rogers RT/duroid 5880 was used as the substrate. (c) Final HFSS model of the metamaterial lens with the monopole feed. The inset shows the monopole located at the middle of the lens. (d) Photograph of the fabricated lens. The inset is an enlarged photograph of the inner layers of the lens with monopole inside.

III. Metamaterial Realization of the Quad-Beam Lens for Monopole Antenna

To experimentally verify the proposed multi-beam directive emission coordinate transformation, a quad-beam metamaterial lens was designed that tailors the radiation of a G-band quarter-wavelength monopole which nominally radiates omnidirectionally in the *H*-plane around 4 to 5 GHz [32]. Because the radiated electric fields are nearly perpendicular to the ground plane in the *H*-plane, the lens needs only to work for the *TE* polarization. Following the configuration of the two-dimensional quad-beam lens example in Fig. 2(b), the monopole is surrounded with four triangular anisotropic metamaterial lens segments as presented in Fig. 5(a). Segments 1 and 3 have a low value of effective μ_{rx}, and segments 2 and 4 have a low value of effective μ_{ry}.

A. Unit Cell Design

To design an anisotropic metamaterial with one specific effective permeability tensor parameter having a low value in the G-band, broadside coupled capacitor loaded ring resonators (CLRRs) made of copper [37] are utilized as the building blocks. The geometry of the unit cell is shown in Fig. 5(b). The CLRRs are printed on each side of the dielectric substrate. The openings of the CLRRs are oriented in opposite directions to eliminate any bi-anisotropy that might be caused by the structural asymmetry [54].

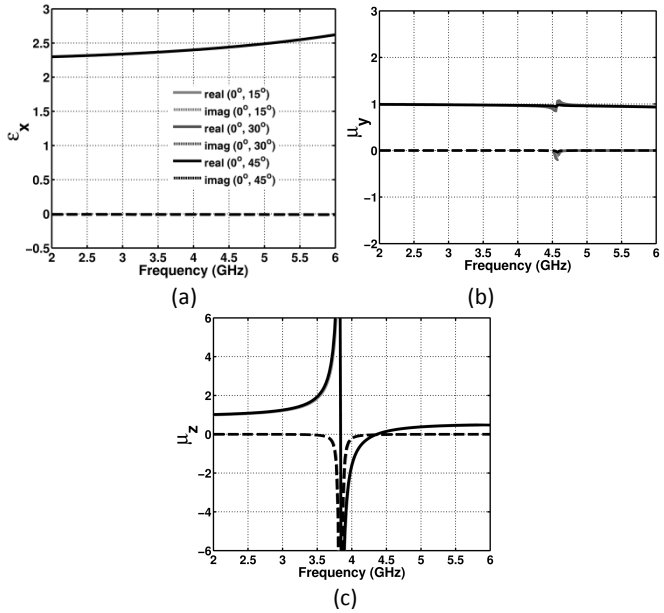

Fig. 6. Retrieved effective medium parameters (a) ε_x, (b) μ_y and (c) μ_z using scattering parameters calculated at different angles of incidences. The legend indicates the two angles of incidence used for each set of curve.

The metamaterial building block was designed using Ansoft HFSS™, where the scattering parameters were calculated through the application of periodic boundary conditions assigned to the lateral walls in both *x*- and *y*-directions. A *TE* polarized plane wave (contained in the *y*-*z* plane with the electric field along the *x*-direction) is assumed to be incident from the upper half-space at an angle $\theta_i (0° \leq \theta_i \leq 90°)$ with respect to the axis of the metamaterial $\hat{z}$. Three layers of unit cells were used in the *z*-direction in order to take into consideration the coupling between adjacent layers, thus enabling the acquisition of more accurate effective medium parameters. The three material tensor parameters active under *TE* polarized illumination (μ_y, μ_z and ε_x), which can be retrieved using a generalized anisotropic inversion algorithm [55], are shown plotted in Fig. 6(a)-(c). It is observed that the inverted metamaterial parameters extracted from the scattering parameters calculated at different angles of incidence agree well with each other, indicating an angularly independent anisotropic effective medium property. Fig. 6(a) and Fig. 6(b) show that ε_x and μ_y are weakly dispersive and do not resonate in the band of interest. This provides a stable normalized impedance for waves propagating in the *z*-direction, *i.e.* the direction of the outgoing beam in the directive emission coordinate transformation. Additionally, the lens is nearly matched to free space ($\sqrt{\mu_y/\varepsilon_x} \approx 0.7$), ensuring low reflection at the lens-air interface. In contrast, the longitudinal tensor parameter μ_z has a strong Lorentz-shaped resonance at 3.8 GHz and maintains a low value ($0 \leq |\mu_z| \leq 0.4$) throughout the resonance tail over a broad bandwidth (4.2 GHz ~ 5.3 GHz) with a weakly dispersive profile. This low μ_z region, located away from the resonance band, is very low loss with the magnitude of $\mathrm{Im}\{\mu_z\}$ less than 0.04.

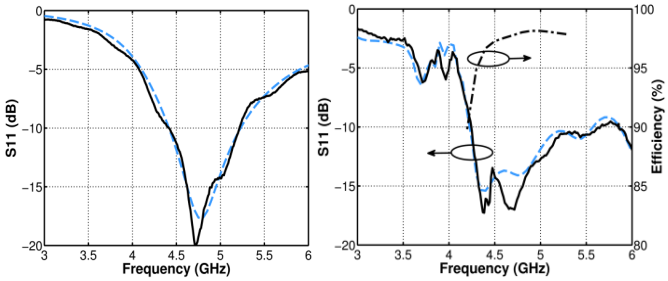

Fig. 7. Simulated (- - - - -) and measured (——) S_{11} of the monopole antenna (a) without the metamaterial lens, and (b) with the metamaterial lens. The simulated efficiency is also shown in (b).

B. Integrated Lens Simulation

The configuration of the final quad-beam lens with the monopole feed and actual metamaterial layers is shown in Fig. 5(c). The constructed lens is composed of nine concentric anisotropic capacitor loaded ring resonator (CLRRs) layers. The square-shaped layers are each five unit cells tall and decrease in edge length by two unit cells for each successive layer starting from the outside of the lens and moving inward. The length of the outer edge of the lens is 102 mm or about 1.6λ at 4.7 GHz, while the height of the lens is 30 mm, about 0.5λ at 4.7 GHz. For segments 1 and 3, the axis of the CLRRs is along the *x*-direction, thereby providing a low value of effective μ_{rx}. Conversely, for segments 2 and 4, the axis of the CLRRs is along the *y*-direction, which yields a low value of effective μ_{ry}. A monopole with a length of 14.5 mm is located in the middle of the lens as shown in the inset of Fig. 5(c). A 14 cm by 14 cm (~2λ × 2λ) brass plate is used as the ground plane. Copper is used for the metallic patterns to account for the loss resulting from finite conductivity.

The simulated S_{11} of the monopole with and without the lens is shown in Fig. 7(a) and Fig. 7(b). For the monopole alone, it has a single resonance at 4.8 GHz with a -10 dB bandwidth of around 0.78 GHz (4.42 GHz ~ 5.20 GHz). However, with the lens present, the -10 dB S_{11} bandwidth is increased to 1.35 GHz (4.20 GHz ~ 5.55 GHz), an increase of about 70%. This can be attributed to two causes, the first being an effective ε_{rz} (*i.e.* ε_x shown in Fig. 6(c)) having a value weakly growing from 2.3 to around 2.7, dropping the quality factor of the monopole resonance. Hence, the S_{11} curve is not as sharp as that of the monopole alone at higher frequency. Secondly, the near-field coupling between the monopole and the unit cells on the inner layers of the lens is tuned such that multiple resonances can be observed at 4.3 GHz, 4.75 GHz and 5.4 GHz. These resonances pull the S_{11} below -10 dB over a much broader bandwidth.

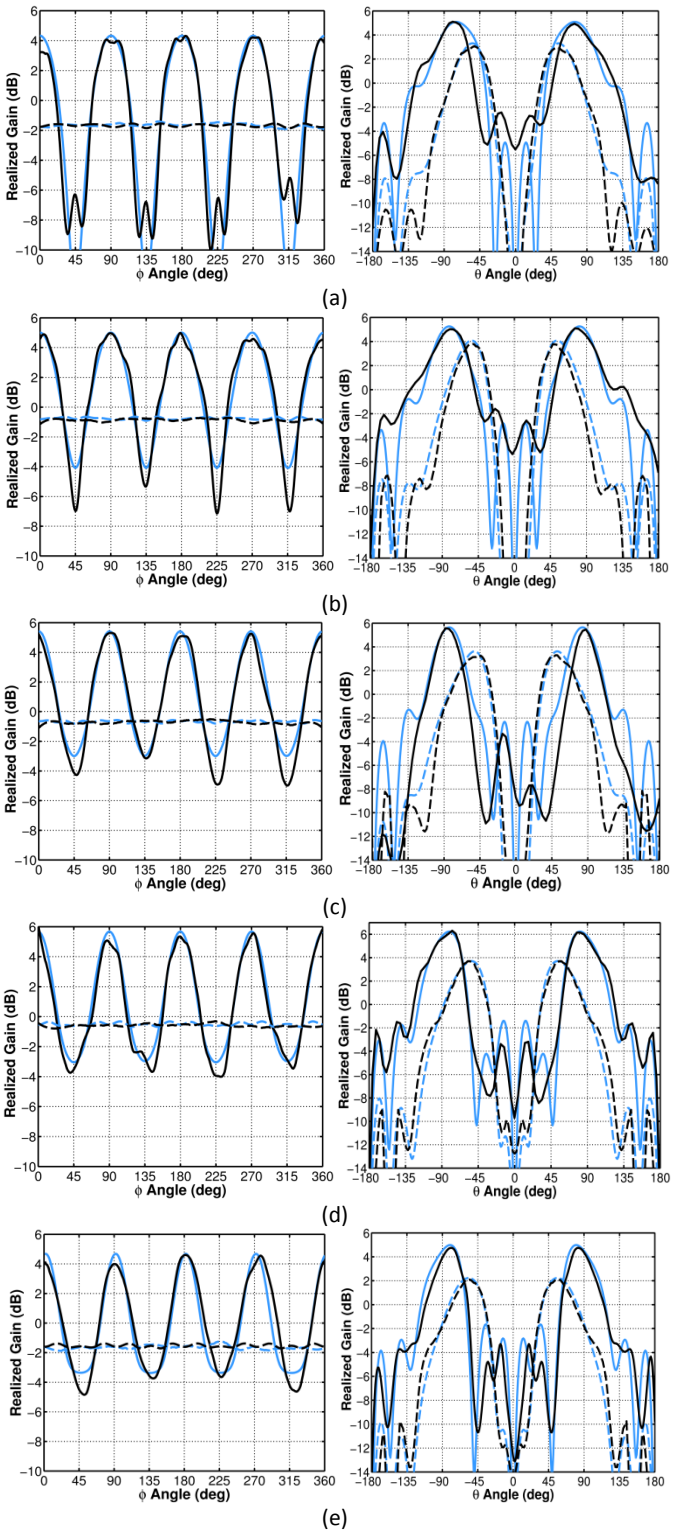

Fig. 8. Simulated and measured *H*-plane (left) and *E*-plane (right) realized gain patterns of the monopole antenna with and without the metamaterial lens at (a) 4.25 GHz, (b) 4.50 GHz, (c) 4.85 GHz, (d) 5.10 GHz, and (e) 5.30 GHz. The legends represent simulation without the lens (- - - - -), simulation with the lens (——), measurement without the lens (------), measurement with the lens (——).

Fig. 8(a)-(e) (left, blue curves) show the simulated realized gain patterns in the *H*-plane of the monopole with and without the lens at 4.25 GHz, 4.50 GHz, 4.85 GHz, 5.10 GHz and 5.30 GHz. Without the lens, the monopole exhibits an omni-directional

pattern in the *x*-*y* plane with a variation of about 0.7 dB due to the finite ground plane size. The maximum realized gain varies within the range from -1.5 dB to -0.3 dB as the frequency increases. With the lens, however, four highly directive beams can be observed at 0°, 90°, 180° and 270°. Within the frequency band of 4.20 GHz to 5.30 GHz, the peak realized gain of the four beams grows from 4.3 dB to 5.8 dB, about 5.8 ~ 6.1 dB higher than that of the monopole alone. The half-power beam widths (HPBW) of the four directive beams are approximately 35°, 34°, 32°, 30° and 32° at the five frequencies.

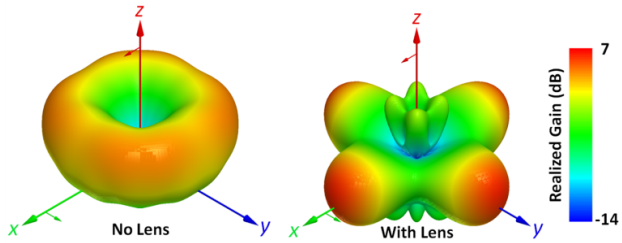

Fig. 9. Simulated 3D realized gain pattern of the monopole antenna with and without the metamaterial lens at 5.10 GHz.

The realized gain pattern in the *E*-plane (the elevation plane) is also investigated. In Fig. 8(a)-(e) (right, blue curves), the simulated gain patterns in the *y*-*z* (ϕ=90°) plane with and without the lens are plotted. Without the lens, the monopole has maximum radiation at around 40° from the horizon ($\theta = 90°$) and nulls along the *z*-direction ($\theta = 0°$) due to the finite ground plane. The metamaterial lens, on the other hand, redirects the maximum of the radiated beam in a direction closer to the horizon (*i.e.* only about 6°-10° above the horizon in the range of 4.25-5.30 GHz) where receivers are usually located. The *E*-plane HPBW is also narrowed from 51-60° to 35-41° in the range of 4.25-5.30 GHz. This effect shows that the lens not only effectively transforms a two dimensional cylindrical wave into four collimated waves in the *H*-plane, but also pushes the radiated beam towards the horizon in the third dimension. It is noted that the ground plane size, which is about 2λ by 2λ, is the same for comparisons with and without the metamaterial lens.

The simulated 3D radiation patterns at 5.10 GHz (see Fig. 9) clearly show that the bowl shaped pattern is transformed into four well-collimated beams pointing in directions near the horizon. The simulated efficiency within the band of interest (4.25-5.30 GHz) is plotted in Fig. 7(b). Since the metamaterial lens is operating away from resonance, it does not introduce a significant amount of loss, thus maintaining an efficiency above 90% throughout the band.

To examine the near-field effect of the lens, the electric field distributions on the ground plane are shown with and without the metamaterial TO lens at the five frequencies denoted in Fig. 10(a)-(e). It is clearly seen that the monopole alone gives a circular field distribution, thus leading to a nearly omni-directional far-field pattern in the *H*-plane. However, with the lens, the field pattern becomes a square shape even at close proximity to the source, which corresponds well with the theoretical homogeneous lens simulation presented in Section II. The square shaped field pattern further gives rise to the four highly directive radiated beams, indicating that the metamaterial lens is effectively functioning as a multi-beam collimator, even in the near-field region inside the lens. It is also noticed that the electric field intensity is much stronger with the lens than for the case without the lens, which in turn explains the higher gain observed in the far-field region. As frequency increases, the value of the corresponding effective permeability tensor parameter grows, thus a gradual transition from a circular to near-square pattern is observed in the electric field distributions (Fig. 10(d)-(e)). This degraded collimating performance in the near-field region also accounts for the radiation bandwidth which is slightly narrower than the impedance bandwidth of the system. Examination of the fields demonstrate that the discrete metamaterial implementation of the lens behaves as an effective homogeneous anisotropic medium with certain permeability tensor parameters having a low, near-zero value.

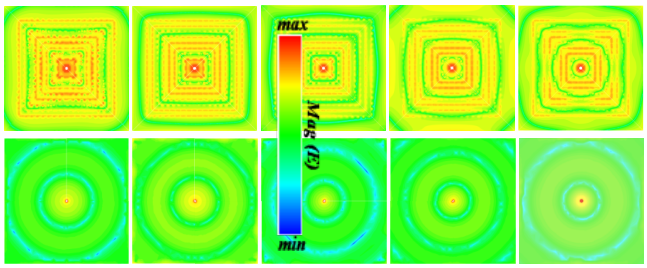

Fig. 10. Electric field distribution on the ground plane with and without the metamaterial TO lens at (a) 4.25 GHz, (b) 4.50 GHz, (c) 4.85 GHz (d) 5.10 GHz and (e) 5.30 GHz.

C. *Experimental Results*

A lens prototype and a monopole antenna platform were fabricated and characterized to validate the theory and numerical design of the transformation optics lens. The fabricated sample is presented in Fig. 5(d) with an enlarged inset figure showing the inner monopole antenna. An Agilent E8364B network analyzer was used to characterize the reflection coefficient magnitude of the monopole with and without the lens. As the results in Fig. 7(a) and Fig. 7(b) show, good agreement can be found between simulations and measurements not only in terms of the -10dB bandwidth but also the resonance positions. The measured S_{11} of the monopole alone has a resonance at 4.75 GHz, with a -10 dB bandwidth of 0.76 GHz (4.42 GHz ~ 5.18 GHz). When the monopole is surrounded by the metamaterial lens, the measured S_{11} is below -10 dB from 4.22 GHz to 5.60 GHz with three resonances located at 4.35 GHz, 4.7 GHz and 5.45 GHz, exhibiting strong correspondence with the simulated results. Even at low frequencies, good agreement is observed in the minor resonances around 3.7 GHz and 3.95 GHz, which can be attributed to the near field coupling to the lens.

The realized gain patterns of the monopole antenna with and without the lens were characterized in an anechoic chamber with an automated antenna movement platform. In Fig. 8(a)-(e) (black curves), the measured gain patterns in both the *H*-plane and *E*-plane at 4.25 GHz, 4.50 GHz, 4.85 GHz, 5.10 GHz and 5.30 GHz are shown, where good agreement is seen with the simulated results. The discrepancies are primarily due to minor inaccuracies in fabrication, non-ideal effects of the test setup, and noise in measurement. For the case without the metamaterial lens, the monopole has a nearly omni-directional radiation pattern in this band. The maximum measured realized gain values in the *H*-plane vary between -1.6 dB to -0.3 dB. With the lens present, four high gain beams are located at 0°, 90°, 180° and 270° with a measured realized gain varying between the range from 4.3 dB to 5.9 dB, yielding about 5.9 dB to 6.2 dB of realized gain improvement. The measured average HPBWs of the four directive beams are approximately 36°, 37°, 30°, 31° and 34° at the five frequencies considered. The measured *E*-plane patterns confirm the beam bending effect in the ϑ-direction. Without the lens, the monopole alone has a measured beam maxima moving from 45° to 40° off horizon as the frequency increases. With the lens present, the beam maxima is maintained at approximately 8° to 12° from the horizon. In all, the experiment verifies the 3D collimating effect of the metamaterial transformation optics lens in reshaping the radiation of the embedded monopole antenna into multiple highly directive radiated beams. Using a larger sized lens will provide even higher gain and narrower half-power beamwidths which will be discussed below.

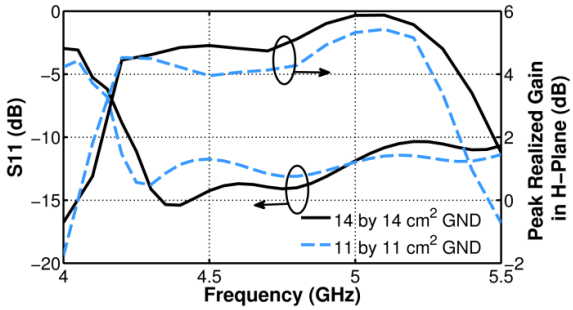

Fig. 11. Simulated S_{11} and peak realized gain in the *H*-plane for the monopole with metamaterial lens on a 14×14 cm^2 (------) and a 11×11 cm^2 (——) ground plane.

IV. Discussions

Several additional simulations were conducted with varied lens parameters in order to gain a more comprehensive understanding of the properties of the metamaterial collimating lens. First, the size of the ground plane was truncated from 14×14 cm^2 to 11×11 cm^2 which is nearly the size of the lens. It can be seen that this has very little impact on the reflection coefficient magnitude (see Fig. 11); the entire antenna system maintains S_{11} below -10 dB in the target band. It is also observed that the radiation bandwidth in the *H*-plane is well maintained with an average drop of only 0.5 dB partially due to the slightly increased reflection at the port and partially attributed to the tilt of beam away from the horizon in the *E*-plane. However, the overall performance is maintained meaning that the lens can still function with a miniaturized footprint.

The impact on the system performance when changing the height and the length of the outer edge of the lens is also investigated. Three metamaterial lenses with four, five, and six layers in the *z*-direction, corresponding to height values of 24mm, 30mm, and 36mm were simulated. The simulated S_{11} and peak realized gain in the *H*-plane are plotted in Fig. 12(a). The return losses are greater than 10 dB within the band of interest for all three lenses; improvement is seen by increasing the height of the lens. For the realized gain in the *H*-plane, increasing the height of the lens gives more enhancement due to larger aperture size and bending of the radiated beams towards the horizon as shown in Fig. 12(b). Without the lens, the beam

maximum is 33-38° from the horizon. By adding the lens, the beam maximum is pushed significantly towards horizon as shown in Fig. 8 and Fig. 9. The thicker the lens, the closer the beam maximum becomes to the horizon.

When the length of the outer edge of the lens is changed, S_{11} is still maintained below -10 dB within the band of interest. The realized gain generally increases with a wider lens due to the larger aperture. The maximum realized gain moves lower in the frequency band due to the fact that, at high frequencies (when the lens is larger than two wavelengths), the aperture does not maintain a perfect equi-amplitude and equi-phase field distribution. Hence, the collimating effect is degraded, leading to a drop in gain. The optimum length has to be chosen so that increased realized gain is achieved within the band of interest, while S_{11} is also below -10 dB.

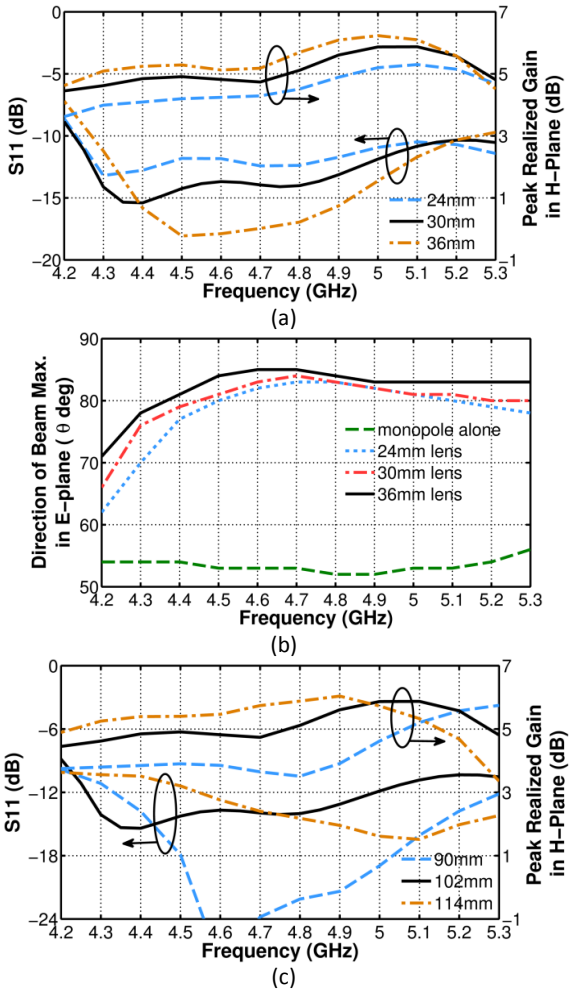

Fig. 12. (a) Simulated S_{11} and peak realized gain in the *H*-plane for the monopole and metamaterial lens combination with various heights. (b) Simulated direction of beam maximum in the *E*-plane for the monopole and metamaterial lens combination with various heights and the monopole alone. (c) Simulated S_{11} and peak realized gain in the *H*-plane for the monopole and metamaterial lens combination with various length values of the outer edge.

V. Conclusions

In conclusion, we have proposed two- and three-dimensional embedded coordinate transformations that generate multiple highly directive radiated beams from an embedded isotropic source, each pointing in a desired direction. The coordinate transformation introduced here offers anisotropic but spatially invariant material parameters that can be readily implemented by metamaterial building blocks. In addition, the performance of the coordinate transformation is not sensitive to small variations in the material parameter values, thus enabling broad operating bandwidth. A microwave frequency metamaterial lens fed by a simple monopole antenna was designed, fabricated and tested, exhibiting strong agreement between simulation and measurement. The metamaterial lens achieves a quad-beam radiation pattern over a 1.26:1 bandwidth with around 5.9 to 6.2 dB of realized gain improvement in the *H*-plane compared to the monopole alone. Additionally, it broadens the impedance bandwidth of the monopole by 70%. The simple coordinate transformation suggests possibilities for the design and synthesis of more practical broadband metamaterial devices, including lenses that are able to tailor the radiation properties of microwave/millimeter wave wireless antennas and even perhaps optical nano-antennas [56].

ACKNOWLEDGMENT

This work was supported by the National Science Foundation (NSF) Materials Research Science and Engineering Center (MRSEC) Grant No. DMR-0213623. This work is also supported by Autonomous Province of Trento - Calls for proposal "Team 2011".

The authors gratefully acknowledge Dr. Qi Wu for fruitful discussions.

REFERENCES

[1] J. B. Pendry, D. Schurig, and D. R. Smith, "Controlling electromagnetic fields," *Science*, vol. 312, no. 5781, pp. 1780-1782, May 2006.
[2] U. Leonhardt, "Optical conformal mapping," *Science*, vol. 312, no. 5781, pp. 1777-1780, May 2006.
[3] D.-H. Kwon and D. H. Werner, "Transformation electromagnetics: An overview of the theory and applications," *IEEE Antennas Propag. Mag.*, vol. 52, no. 1, pp. 24-46, Feb. 2010.
[4] H. Chen, C. T. Chan, and P. Sheng, "Transformation optics and metamaterials," *Nat. Mater.*, vol. 9, no. 4, pp. 387-396, Apr. 2010.
[5] N. Kundtz, D. R. Smith, and J. B. Pendry, "Electromagnetic design with transformation optics," *Proc. IEEE*, vol. 99, no. 10, pp. 1622-1633, Oct. 2011.
[6] D. Schurig, J. J. Mock, B. J. Justice, S. A. Cummer, J. B. Pendry, A. F. Starr, and D. R. Smith, "Metamaterial electromagnetic cloak at microwave frequencies," *Science*, vol. 314, no. 5801, pp. 977-980, Nov. 2006.
[7] E. Semouchkina, D. H. Werner, G. B. Semouchkin and C. Pantano, "An infrared invisibility cloak composed of glass," *Appl. Phys. Lett.*, vol. 96, pp. 233503(1)-(3), Jun. 2010.
[8] H. Chen, B. Hou, S. Chen, X. Ao, W. Wen, and C. T. Chan, "Design and experimental realization of a broadband transformation media field rotator at microwave frequencies," *Phys. Rev. Lett.*, vol. 102, pp. 183903(1)-(4), May 2009.
[9] D.-H. Kwon and D. H. Werner, "Polarization splitter and polarization rotator designs based on transformation optics," *Opt. Express*, vol. 16, no. 23, pp. 18731-18738, Oct. 2008.
[10] M. Rahm, S. A. Cummer, D. Schurig, J. B. Pendry, and D. R. Smith, "Optical design of reflectionless complex media by finite embedded coordinate transformations," *Phys. Rev. Lett.*, vol. 100, pp. 063903(1)-(4), Feb. 2008.
[11] M. Rahm, D. Schurig, D. A. Roberts, S. A. Cummer, D. R. Smith, and J. B. Pendry, "Design of electromagnetic cloaks and concentrators using form-invariant coordinate transformations of Maxwell's equations," *Photon. Nanostruct. Fundam. Appl.*, vol. 6, no.1, pp. 87-95, Aug. 2007.
[12] W. X. Jiang, T. J. Cui, Q. Cheng, J. Y. Chin, X. M. Yang, R. Liu, and D. R. Smith, "Design of arbitrary shaped concentrators based on conformally optical transformation of nonuniform rational B-spline surfaces," *Appl. Phys. Lett.*, vol. 92, pp. 264101(1)-(3), Jun. 2008.
[13] W. X. Jiang, T. J. Cui, H. F. Ma, X. Y. Zhou, and Q. Cheng, "Cylindrical-to-plane-wave conversion via embedded transformation," *Appl. Phys. Lett.*, vol. 92, pp. 261903(1)-(3), Jul. 2008.
[14] J. J. Zhang, Y. Luo, S. Xi, H. S. Chen, L. X. Ran, B.-I. Wu, and J. A. Kong, "Directive emission obtained by coordinate transformation," *PIERS*, vol. 81, pp. 437-446, 2008.
[15] D.-H. Kwon and D. H. Werner, "Transformation optical designs for wave collimators, flat lenses and right-angle bends," *N. J. Phys.*, vol. 10, pp. 115023(1)-(13), Nov. 2008.
[16] P.-H. Tichit, S. N. Burokur, D. Germain, and A. Lustrac, "Design and experimental demonstration of a high-directive emission with transformation optics," *Phys Rev. B.*, vol. 83, pp. 155108(1)-(7), Apr. 2011.
[17] Y. Luo, J. Zhang, H. Chen, J. Huangfu, and L. Ran, "High-directivity antenna with small antenna aperture," *Appl. Phys. Lett.*, vol. 95, pp. 193506(1)-(3), Nov. 2009.
[18] D. R. Roberts, M. Rahm, J. B. Pendry, and D. R. Smith, "Transformation-optical design of sharp waveguide bends and corners," *Appl. Phys. Lett.*, vol. 93, pp. 251111(1)-(3), Dec. 2008.
[19] W. X. Jiang, H. F. Ma, Q. Cheng, and T. J. Cui, "Illusion media: generating virtual objects using realizable metamaterials," *Appl. Phys. Lett.*, vol. 96, pp. 121910(1)-(3), Mar. 2010.
[20] W. X. Jiang and T. J. Cui, "Radar illusion via metamaterials," *Phys. Rev. E*, vol. 83, pp. 026601(1)-(7), Feb. 2011.
[21] W. Tang, C. Argyropoulos, E. Kallos, W. Song, and Y. Hao, "Discrete coordinate transformation for designing all-dielectric flat antennas," *IEEE Trans. Antennas Propag.*, vol. 58, no. 12, pp. 3795-3804, Dec. 2010.
[22] D. R. Smith and D. Schurig, "Electromagnetic wave propagation in media with indefinite permittivity and permeability tensors," *Phys. Rev. Lett.*, vol. 90, pp. 077405(1)-(4), Feb. 2003.
[23] N. Engheta and R. W. Ziolkowski, *Metamaterials: Physics and Engineering Explorations*. Wiley-IEEE Press, Jun. 2006.
[24] J. Li and J. B. Pendry, "Hiding under the carpet: A new strategy for cloaking," *Phys. Rev. Lett.*, vol. 101, pp. 203901(1)-(4), Nov. 2008.
[25] R. Liu, C. Ji, J. J. Mock, J. Y. Chin, T. J. Cui, and D. R. Smith, "Broadband ground-plane cloak," *Science*, vol. 323, no. 5912, pp. 366-369, Jan. 2009.
[26] J. Valentine, J. Li, T. Zentgraf, G. Bartal, and X. Zhang, "An optical cloak made of dielectrics," *Nat. Mater.*, vol. 8, no. 7, pp. 568-571, Jul. 2009.
[27] N. Kundtz and D. R. Smith, "Extreme-angle broadband metamaterial lens," *Nat. Mater.*, vol. 9, no. 12, pp. 129-132, Dec. 2009.
[28] H. F. Ma and T. J. Cui, "Three-dimensional broadband and broad-angle transformation-optics lens," *Nat. Commun.*, vol. 1, pp. 124(1)-(7), Nov. 2010.
[29] L. M. Zhong and T. J. Cui, "Experimental realization of a broadband bend structure using gradient index metamaterials," *Opt. Express*, vol. 17, no. 20, pp. 18354-18363, Sept. 2009.
[30] B. Zhang, Y. Luo, X. Liu and G. Barbastathis, "Macroscopic invisibility cloak for visible light," *Phys. Rev. Lett.*, vol. 106, pp. 033901(1)-(4), Jan. 2011.
[31] X. Chen, Y. Luo, J. Zhang, K. Jiang, J. B. Pendry, and S. Zhang, "Macroscopic invisibility cloaking of visible light," *Nat. Commun.*, vol. 2, pp. 176(1)-(6), Feb. 2011.
[32] C. A. Balanis, *Modern Antenna Theory: Analysis and Design*, John Wiley & Sons, NY, 2008.
[33] W. L. Stutzman and E. L. Coffey, "Radiation pattern synthesis of planar antennas using the iterative sampling method," *IEEE Trans. Antennas Propag.*, vol. 23, no. 6, pp. 764-769, Nov. 1975.
[34] P. Nayeri, F. Yang, and A. Z. Elsherbeni, "Design and experiment of a single-feed quad-beam reflectarray antenna," *IEEE Trans. Antennas Propag.*, vol. 60, no. 2, pp. 1166-1171, Feb. 2012.
[35] L. Zhou, H. Li, Y. Qin, Z. Wei, and C. T. Chan, "Directive emission from subwavelength metamaterial-based cavities," *Appl. Phys. Lett.*, vol. 86, pp. 101101(1)-(3), Jun. 2005.
[36] N. Guérin, S. Enoch, G. Tayeb, P. Sabouroux, P. Vincent, and H. Legay, "A metallic fabry-perot directive antenna," *IEEE Trans. Antennas Propag.*, vol. 54, no. 1, pp. 220-224, Jan. 2006.
[37] A. Erenok, P. L. Luljak, and R. W. Ziolkowski, "Characterization of a volumetric metamaterial realization of an artificial magnetic conductor for antenna applications," *IEEE Trans. Antennas Propag.*, vol. 53, no. 1, pp. 160-172, Jan. 2005.

[38] A. P. Feresidis, G. Goussetis, S. Wang, and J. C. Vardaxoglou, “Artificial magnetic conductor surfaces and their application to low-profile high-gain planar antennas,” *IEEE Trans. Antennas Propag.*, vol. 53, no. 1, pp. 209-215, Jan. 2005.
[39] C. Cheype, C. Serier, M. Thèvenot, T. Monédière, A. Reineix, and B. Jecko, “An electromagnetic bandgap resonator antenna,” *IEEE Trans. Antennas Propag.*, vol. 50, no. 9, pp. 1285-1290, Sep. 2002.
[40] F. Yang and Y. Rahmat-Samii, “Reflection phase characterization of the EBG ground plane for low profile wire antenna applications,” *IEEE Trans. Antennas Propag.*, vol. 51, no. 10, pp. 2691-2703, Oct. 2003.
[41] S. Enoch, G. Tayeb, P. Sabouroux, N. Guérin, and P. Vincent, “A metamaterial for directive emission,” *Phys. Rev. Lett.*, vol. 89, pp. 213902(1)-(4), Nov. 2002.
[42] R. W. Ziolkowski, “Propagation in the scattering from a matched metamaterial having a zero index of refraction,” *Phys. Rev. E*, vol. 70, pp. 046608(1)-(12), Oct. 2004.
[43] I. Bulu, H. Caglayan, K. Aydin, and E. Ozbay, “Compact size highly directive antennas based on the SRR metamaterial medium,” *N. J. Phys.*, vol. 7, pp. 223(1)-(10), Nov. 2005.
[44] Y. Yuan, L. Shen, L. Ran, T. Jiang, J. Huangfu, and J. A. Kong, “Directive emission based on anisotropic metamaterials,” *Phys. Rev. A*, vol. 77, pp. 053821(1)-(5), May 2008.
[45] J. P. Turpin, A. T. Massoud, Z. H. Jiang, P. L. Werner, and D. H. Werner, “Conformal mappings to achieve simple material parameters for transformation optics devices, ” *Opt. Express*, vol. 18, no. 1, pp. 244-252, Jan. 2010.
[46] R. Zhou, H. Zhang, and H. Xin, “Metallic wire array as low-effective index of refraction medium for directive antenna application,” *IEEE Trans. Antennas Propag.*, vol. 58, no. 1, pp. 79-87, Jan. 2010.
[47] Z. H. Jiang, M. D. Gregory, and D. H. Werner, “Experimental demonstration of a broadband transformation optics lens for highly directive multibeam emission,” *Phys. Rev. B*, vol. 84, pp. 165111(1)-(6), Oct. 2011.
[48] J. A. Kong, *Electromagnetic Wave Theory*, EMW Cambridge, MA, 2000.
[49] H. David, *New Foundations for Classical Mechanics*, Kluwer Academic Publishers, 1999.
[50] http://www.comsol.com/
[51] E. Lier, D. H. Werner, C. P. Scarborough, Q. Wu, and J. A. Bossard, “An octave-bandwidth negligible-loss radiofrequency metamaterial,” *Nat. Mater.*, vol. 10, no. 3, pp. 216-222, Mar. 2011.
[52] C. Cho, H. Choo, and I. Park, “Printed symmetric inverted-F antenna with a quasi-isotropic radiation pattern,” *Microw. Opt. Technol. Lett.*, vol. 50, no. 4, pp. 927-930, Apr. 2008.
[53] http://www.ansoft.com/products/hf/hfss/
[54] R. Marqués, F. Mesa, J. Martel, and F. Medina, “Comparative analysis of edge- and broadside- coupled split ring resonators for metamaterial design-theory and experiments,” *IEEE Trans. Antennas Propag.*, vol. 51, no. 10, pp. 2572-2581, Oct. 2003.
[55] Z. H. Jiang, J. A. Bossard, X. Wang, and D. H. Werner, “Synthesizing metamaterials with angularly independent effective medium properties based on an anisotropic parameter retrieval technique coupled with a genetic algorithm,” *J Appl. Phys.*, vol. 109, pp. 013515(1)-(11), Jan. 2011.
[56] L. Novotny and N. Hulst, “Antennas for light,” *Nat. Photon.*, vol. 5, pp. 83-90, Feb. 2011.